Quantifying microstructural contribution to yield stress and strain hardening of Ni20Cr alloy manufactured by laser powder bed fusion with different volumetric energy densities

Shubham Sanjay Joshi [1], Clément Keller [2], Eric Hug [3], Williams Lefebvre [1]
[1] Groupe de Physique des Matériaux, Normandie Université, INSA de Rouen Normandie, Université de Rouen, UMRCNRS 6634, Saint-Etienne du Rouvray, France
[2] Laboratoire Génie de Production, INP-ENIT, Tarbes, France
[3] Laboratoire CRISMAT, Normandie Université, Université de Caen, UMRCNRS 6508, Caen, France

Abstract: Laser powder bed fusion (LPBF) process is an additive manufacturing technique that focuses on intricate metal fabrication using laser processing of metallic powder. Various processing parameters like laser power, scanning speed, and hatch spacing giving out unique applied volumetric energies are involved in such fabrication. Those varied energies bring about microstructural changes leading to modifications in mechanical response such as yield stress and strain hardening behaviour. In this work, we investigated the influence of volumetric energy density on the aforementioned mechanical properties of a Ni-20 wt%Cr alloy manufactured via LPBF. First, an analytical model was employed to study the contribution of each microstructural feature on yield stress of LPBF samples. Dendritic cellular structures (and their sizes) are found to be the most important feature to govern this parameter. The Kocks-Mecking model was further extended to associate the different strain hardening mechanisms with dislocation production and interaction mechanisms via different channels like dendritic cellular structures, grains and forest dislocations. The production of dislocation via dendritic cellular structures is also the most significant mechanism for unique hardening behaviour in LPBF alloys. A modified equation of dislocation production mechanisms is finally proposed to simplify the application of this model for modelling the mechanical behaviour in tension of LPBF Ni20Cr.

Keywords: Additive manufacturing, volumetric energy, Kocks-Mecking model, mechanical properties, microstructure, Ni-alloys

1. Introduction

Recently, new avenues for a scrap-free and lightweight design fabrication have emerged as a result of the development of additive manufacturing (AM) processes [1]-[2]. Laser Powder Bed Fusion (LPBF) process is one of the techniques of AM dealing with metal powder as a feedstock to build complex parts. Process parameters like laser power, hatch spacing, laser scanning speed, powder layer thickness deliver unique applied Volumetric Energy Densities (VEDs) as input during laser melting [3]. These parameters are optimized so as to fabricate parts with least porosity possible. LPBF is a layer-by-layer manufacturing process meaning that every layer of powder is melted with the help of laser and further solidified, henceforth the laser inputs such volumetric energy to melt every layer of powder [4]. Therefore, formerly solidified powder layers below undergo repetitive heating-cooling cycles. LPBF process, due to this rapid melting and solidification and out of equilibrium process conditions, induces unique microstructure like heterogeneous grain structure, columnar dendrites, dendritic cellular structures, high dislocation density, precipitates, meltpools. These microstructural features have a strong impact on mechanical properties. Donik et al. [5] reviews how grain size [3]-[4], meltpool dimensions

This article has been published in Journal of Alloys and Compounds. The edited version of the article can be found here: https://doi.org/10.1016/j.jallcom.2023.172241

[6], dislocation cell walls [8], and texture [3][5] are associated with the process parameters and several studies were evaluated focussing on each feature of multiscale microstructure. Aforementioned process parameters combined with scanning strategies, scanning angle, etc. are considered to be responsible for such a microstructure. Many VEDs with different sets of process parameters can induce 'minimum' porosity parts which may fulfil industry criteria. However, with change in VEDs, it is possible to bring about microstructural changes in the fabricated parts. Mechanical properties of LPBFed materials are directly connected to the generated microstructure. So, selection of VEDs or tailoring the microstructure depends on desired mechanical properties. Intensive studies have been, hence, performed to investigate the process-microstructure-properties link of AM or LPBF [1][6]. Specifically, many such studies investigated the influence of process parameters on microstructure and mechanical properties of AlSi10Mg [10], Al binary alloys [11], NiTi alloy [12], CuCrZr alloy [13], IN718 [14]. Nevertheless, the question of the quantification of the different AM microstructures to mechanical properties is still a remaining question. This quantification is of prime importance to select the VEDs and to tailor the microstructure to achieve desired properties.

In a previous work, the authors employed analytical models such as Taylor or Kocks-Mecking on Ni20Cr fabricated by LPBF process to establish that 43% of yield stress and strain hardening in such alloys come from dendritic cellular structures. In that case, only one VED of 62 J/mm^3 was considered and conclusions may not be extended to other VED or microstructure. In this paper, the objective is to try to generalize the quantification of the microstructure feature to yield stress and strain hardening for different values of VEDs (from 46 J/mm^3 to 231 J/mm^3) generating different microstructures (another possibility could be manoeuvring different sets of parameters, keeping the volumetric energy constant) using similar analytical models and microstructure characterization. Ni20Cr (80 wt.% Ni and 20 wt.%Cr) is employed owing to its rather monophasic character and planar glide (restricted cross-slip) [15]. Moreover, this binary alloy has industrial applications owing to high temperature mechanical properties due to Ni [16] and enhanced corrosion resistance due to Cr [17] and its chemical composition is the base of several nickel superalloys. Results of this article can be then used to help to tailor the microstructure of such alloys for industrial applications manufactured by LPBF.

2. Experimental and numerical procedure

2.1. Material fabrication

Cylindrical samples of Ni20Cr with dimension of 20 mm × 100 mm (diameter × height) were fabricated at the CRISMAT laboratory in Caen, France, using a SLM125HL machine. Cuboids of dimensions 10 mm × 15 mm × 20 mm (length × width × height) were printed for density analysis. Table 1 summarizes different parameter sets giving out unique volumetric energy densities (VEDs). The parameter selection was done in a prior work by Hug and co-authors [18] to reduce porosity and get a range of parameters achieving similar relative densities close or larger than 99%. Volumetric energy density (VED or E_v) can be calculated using a printability map of process parameters like laser power *(P)*, scanning speed *(v)*, hatch distance *(h)*, powder layer thickness *(t)* as follows (eq. 1):

$$E_v = \frac{P}{hvt} \quad (1)$$

This article has been published in Journal of Alloys and Compounds. The edited version of the article can be found here: https://doi.org/10.1016/j.jallcom.2023.172241

Table 1: Optimized parameters used for LPBF fabrication of Ni20Cr specimens.

LPBF parameters	Sample 1	Sample 2	Sample 3	Sample 4	Sample 5
Laser power (W)	150	200	300	300	300
Scanning speed (mm/s)	900	900	900	700	360
Hatch distance (mm)	0.12	0.12	0.12	0.12	0.12
Layer thickness (µm)	30	30	30	30	30
Volumetric energy density (J/mm^3)	**46**	**62**	**90**	**120**	**231**

Moreover, inert gas velocity of 7 m/s (Argon) was used, and stripes was employed to be the scanning strategy with a rotation angle of 67°.

2.2. Microstructural characterization and Mechanical testing

The microstructural characterization was carried out using a Scanning Electron Microscope (JEOL 7900F with secondary electron detector and Electron Back-Scattered Detector (EBSD)) and Scanning Transmission Electron Microscope (STEM) ((JEOL ARM), with a Transmission Electron Microscope (TEM)). For the SEM analysis, the samples were first mechanically ground and polished with SiC abrasive sheets, then they were electropolished in a Struers A2 electrolyte at 15 V for 30 s. Crystal orientation distribution analysis and morphological and crystallographic textures were investigated using electron back-scattered diffraction (EBSD) with a step size of 1.5 µm. With the help of SEM and the Electron Channelling Contrast Imaging (ECCI) method, dendritic cellular structures and dislocations were also imaged. These analyses were carried out at a working distance of 5 mm and a 25 V acceleration voltage. For TEM samples, following mechanical grinding, thin discs of 3 mm in diameter were obtained using a punch hole device, and finally electropolished at 24 V and −40 °C using Struers TenuPol-5 (jet polishing system) with a 90% methanol and 10% perchloric acid electrolyte. The acceleration voltage condition for TEM and STEM systems was 200 kV. For dendritic cellular size analysis, both the slices perpendicular and parallel to the building direction (plane XY and YZ) were considered. Dendrite size analysis was performed using Fiji [19], an open source package built on ImageJ software.

The LPBF samples were built vertically (building direction being parallel to z-axis) in a 'net-shape' condition in a dog bone configuration (with a diameter of 6 mm and a gage length of 24 mm) [18]. These samples were not machined prior to testing. Monotonic tensile tests were conducted at room temperature using an electromechanical tensile machine with a 50 kN load cell in displacement-controlled condition with the help of a "clip-on" extensometer at a mean strain rate of 10^{-3} s^{-1}. Three samples have been tested for each volumetric energy employed to ensure statistical significance of the results.

2.3. Kocks-Mecking model

For conventionally manufactured FCC alloys, Kocks-Mecking (KM) based models have been successfully used in the past to replicate and comprehend the mechanisms of strain hardening independently of the Stacking Fault Energy (SFE) [20]-[21]. It was successfully employed for Ni20Cr alloy fabricated via LPBF in a previous work [15] for one VED of 62 J/mm^3.

This article has been published in Journal of Alloys and Compounds. The edited version of the article can be found here: https://doi.org/10.1016/j.jallcom.2023.172241

The first constitutive equation of the Kocks-Mecking model associates the flow stress, σ, with the dislocation density ρ following the Taylor relationship [21] (eq. 2):

$$\sigma = \sigma_0 + \alpha \mu b M \sqrt{\rho} \quad (2)$$

Where, M is the Taylor factor, b the Burgers vector magnitude, μ is the shear modulus and α is a material parameter considering the dislocation arrangement and the different kinds of interactions between slip systems. σ_0 is an initial stress value denoting the contribution of stress of secondary phases or solid solution hardening. This contribution will be mostly related to former contribution to the flow stress for Ni20Cr. ρ represents the average dislocation density.

The dislocation density evolution rate with plastic strain is represented by the second constitutive equation (eq. 3). When Essmann and Mughrabi first proposed this equation [22], it had two terms: one connected to the storage of dislocations as a result of dislocation interactions, and the other to the processes of annihilating dislocations (via dislocation climb or cross-slip). In recent decades, modifications to the KM model for this particular equation have been proposed [23]–[29], taking into account the contributions of other microstructural features to strain hardening, and can be expressed using eq. 3. All terms in this equation are described in table 2.

$$\frac{d\rho}{d\epsilon_p} = \frac{M\sqrt{\rho}}{\beta b} + \frac{Mk_g}{bd} + \frac{M}{bl_0} - K_2\rho - \frac{M}{bs} + \frac{1}{2eb} \cdot \frac{f_{tw}}{(1-f_{tw})} \quad (3)$$

Table 2: Summary of the values of the different parameters of the Kock-Mecking model identified from modelling of the experimental tensile curves

Right hand term	Contribution type	Details
$\frac{M\sqrt{\rho}}{\beta b}$	Forest dislocation interaction	• β : ratio between the mean free path of gliding dislocations L and the average dislocation distance l (Stage II of hardening)
$\frac{Mk_g}{bd}$	Strain hardening due to GB GNDs	• k_g : material dependent parameter related to grain shape and stacking fault energy [30] • Works when strain mismatches between grains are high. This contribution is crucial in the beginning of plasticity
$\frac{M}{bl_0}$	Initial Dislocations structure	• Due to the presence of initial dislocation structures generated during previous forming processes or to a precipitate network • l_0: initial dislocation structures (associated with dendrite size for LPBF samples) or the average distance between precipitates
$K_2\rho$	Dislocation annihilation	• Third stage of hardening linked to the annihilation of dislocations due to cross-slip or climb during dynamic recovery [22], [31], [32] • K_2 : rate of the annihilation process which depends on the SFE, temperature and stress of the material system

This article has been published in Journal of Alloys and Compounds. The edited version of the article can be found here: https://doi.org/10.1016/j.jallcom.2023.172241

$\frac{M}{bs}$	Dislocation annihilation due to free surfaces	• This rate is governed by the average distance between free surfaces *s* [26] • Only effective for thin samples
$\frac{1}{2eb} \cdot \frac{f_{tw}}{(1-f_{tw})}$	Mechanical twinning	• Impact on strain hardening [23], [33] • e = twin width and f_{tw} = twin fraction; depends on plastic strain • Restricted to low staking fault energy alloys

The conventional one-internal variable (i.e. dislocation density) KM model, which is used in the next sections to assess the role of microstructure on strain hardening, is formed by these two equations, eq. 2 and 3. The numerical tensile curve was computed using a square root optimization technique (Fourth order Range Kutta method) between the experimental data and the numerical tensile curves using a script using the Opensource program Scilab to solve this system of non-linear differential equations [34]. The root mean square deviation is minimized during optimization. The flow stress levels and accompanying strain hardening rate are taken into consideration throughout this minimization.

3. Results and Discussion

3.1. Initial microstructural investigation

Fig. 1 shows SEM observations of the dendritic cellular structure for LPBF Ni20Cr for the five samples with different VEDs in the XY plane (perpendicular to the building direction). The dendrite size for sample with VED of 46 J/mm^3 was found to be close to 0.4 ± 0.05 µm and the trend was found to be increasing with increment in VED. Highest dendrite cell size of 1.08 ± 0.2 µm was observed for sample 5 with highest VED of 231 J/mm^3. Similar trend in the increment in dendritic cellular size was observed in several studies [4]-[5][30].

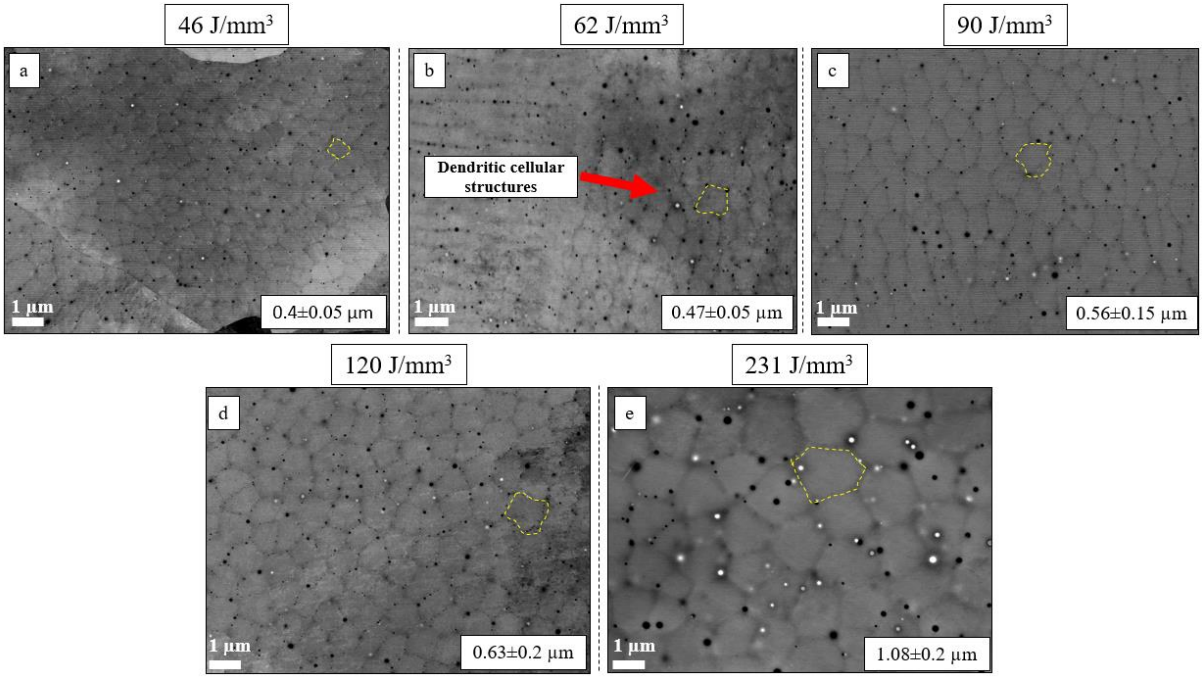

Figure 1: Dendritic cellular structures with average dendrite arm spacing information in the XY plane (plane perpendicular to the building direction) for LPBF Ni20Cr fabricated with a

This article has been published in Journal of Alloys and Compounds. The edited version of the article can be found here: https://doi.org/10.1016/j.jallcom.2023.172241

volumetric energy of (a) 46 J/mm^3, (b) 62 J/mm^3, (c) 90 J/mm^3, (d) 120 J/mm^3, and (e) 231 J/mm^3; Images were obtained in SEM using backscattered electron mode.

The cells represented in fig. 1 are only for illustration purposes; the values depicted in fig. 1 and table 3 are averages of different cell size values. At five separate sample locations, imaging was performed at three different magnifications. The various places were chosen in zones with varying orientations to account for the influence of orientation. Furthermore, where the orientation changes, these cells appear elongated, although they have only rotated according to the direction solidification front and the interdendritic wall distance appears unmodified [36].

These dendritic cellular structures shown in fig. 1 are a part of a colony with same crystallographic orientation which depends upon the directional behaviour of solidification front. Cooling rates ($\dot{T}$) associated with respective dendrite sizes (l_0) can be computed using eq. 4 which is valid for Ni-alloys [37] and subsequent values for all VED samples are given in table 3. The cooling rates reported in this study for LPBF samples with different VEDs are in agreement with literature [13][32]. The black spherical particles are inter-dendritic precipitates of Cr-rich nature also categorized as Cr-rich oxides. Relative density values are also summarized in table 3 using values from a previous work [13].

$$l_0 = 97\dot{T}^{-0.36} \quad (4)$$

Table 3: Dendrite sizes and associated cooling rates for all samples with different VEDs used for LPBF fabrication of Ni20Cr specimens. Errors are given with a confidence index of 95%. Relative density analysis was carried out using Archimedes method and the values are extracted from a previous work [13].

Volumetric energy density (J/mm^3)	Relative density (%)	Dendritic cell size (l_0) (µm)	Cooling rate (10^6 °C/s)
46	98.5	0.40 ± 0.05	4.2 ± 1.2
62	99.1	0.47 ± 0.05	2.7 ± 0.7
90	99.2	0.56 ± 0.2	1.7 ± 0.9
120	99.2	0.63 ± 0.2	1.2 ± 0.6
231	99.1	1.1 ± 0.2	0.27 ± 0.01

Fig. 2 indicates grain orientation maps, pole figures and maximum texture intensities of LPBF Ni20Cr samples built with different VEDs.

This article has been published in Journal of Alloys and Compounds. The edited version of the article can be found here: https://doi.org/10.1016/j.jallcom.2023.172241

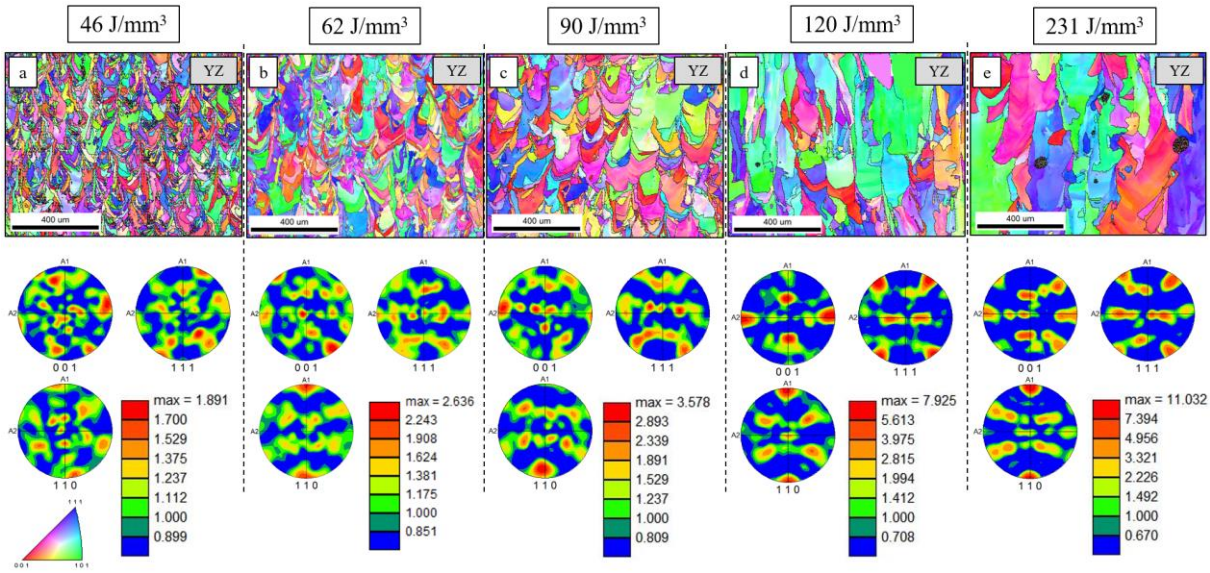

Figure 2: Grain orientation maps and associated pole figures of the LPBF Ni20Cr in the YZ plane (plane parallel to the building direction) which are fabricated with a volumetric energy of (a) 46 J/mm^3, (b) 62 J/mm^3, (c) 90 J/mm^3, (d) 120 J/mm^3, and (e) 231 J/mm^3.

The texture intensity values follow an incrementing trend from 1.9 to 11.03 with increase in VEDs, as also observed for Ni-based Superalloys fabricated by LPBF [39]. Crystallographic texture intensity is relatively low till 90 J/mm^3 but grows extensively from 120 J/mm^3 and highest value is achieved at 231 J/mm^3. Average grain size increases significantly from 30 µm to 200 µm as a function of VED, following the same trend as dendritic cellular structures and texture features. Similar findings are reported for LPBF 316L [5]. Higher VEDs of 120 J/mm^3 and 231 J/mm^3 show predominant columnar grain structures in the building direction. This can be associated to higher thermal gradient and relatively lower cooling rates as shown in table 3 [13][34].

The fraction of low angle grain boundaries (LAGBs) (misorientation <15°) was observed to increase from 60% to 84.3% with increasing VEDs as seen in table 4. Similar trend was reported by Chen et al. for Ni-Superalloy [39]. Barring a huge jump for 62 J/mm^3, there is a steady increment till 231 J/mm^3. Nevertheless, the value is in same order of magnitude for all samples.

Table 4: Grain sizes, maximum texture intensities and fraction of LAGBs associated to all samples with different VEDs used for LPBF fabrication of Ni20Cr specimens

Volumetric energy density (J/mm^3)	Maximum texture intensities	Average grain size (µm)	LAGBs fraction (%) (<15°)
46	1.89	30	60
62	2.63	70	75.5
90	3.58	100	79
120	7.93	130	79.3
231	11.03	200	84.3

Fig. 3 shows how LPBF samples are rich in dislocations in 46 and 231 J/mm^3 (terminal conditions in this study). The heterogeneous dislocation structures are seen in rough cells whose size is observed to be increasing as a function of VED. Similar results were reported in literature

for 316L [5]. Qualitatively, the dislocation density is soft zones are similar for both the samples as seen in fig. 3.

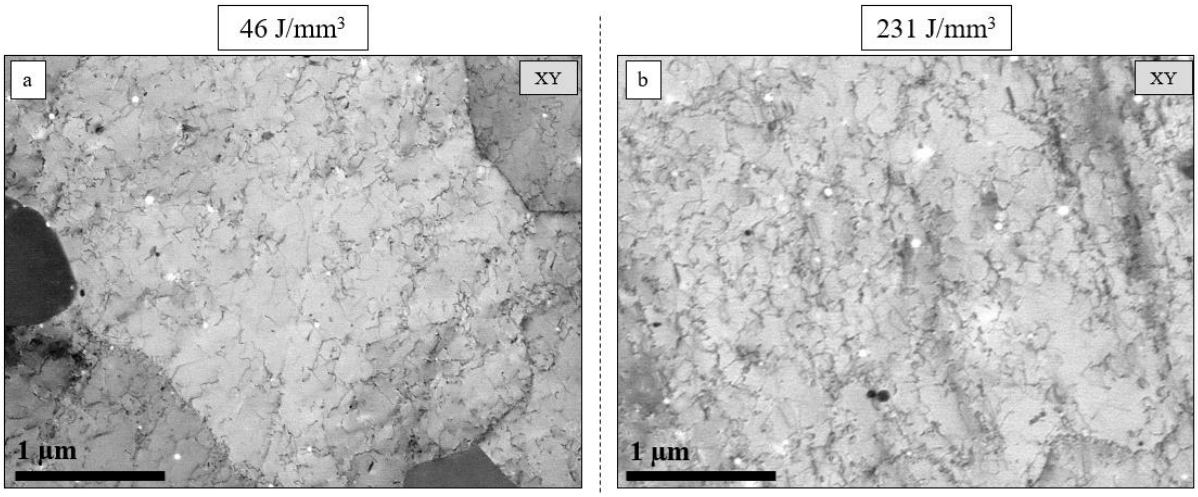

Figure 3: Heterogeneous dislocations structures in the XY plane for LPBF Ni20Cr fabricated with lowest and highest volumetric energies of (a) 46 J/mm3, and (b) 231 J/mm3.

3.2. Monotonic tensile testing

Fig. 4 depicts, in the true stress true strain framework, the tensile curves of LPBF samples fabricated via different VEDs as well as cast Ni20Cr sample for comparison purpose. Yield strength (values given in table 6) is affected by VEDs. Highest yield strength was observed for sample with 62 J/mm^3 (554 MPa) and decreases with increment in VED (till 231 J/mm^3). Similar decrement in YS with increment in VED has been observed for several different materials systems [4][40]. Decreasing YS can be associated to increased cellular size of dislocations or grain size [41]. Yield strength achieved for 46 J/mm^3 (524 MPa) is slightly lower than that of 62 J/mm^3 but can be considered unchanged considering error bar. Same trend has been observed for Ultimate Tensile Strength (UTS) values as LPBF samples with VED of 62 J/mm^3 experiences maximum UTS with clear declining evolution with increasing VEDs, as seen in literature [41]. 'Cyan coloured' curve denotes tensile behaviour of cast Ni20Cr sample with significantly lower yield strength (267 MPa) than all the LPBF samples (least value of 421 MPa for 231 J/mm^3) due to its virgin microstructure at the beginning of the tensile test (recrystallized character).

This article has been published in Journal of Alloys and Compounds. The edited version of the article can be found here: https://doi.org/10.1016/j.jallcom.2023.172241

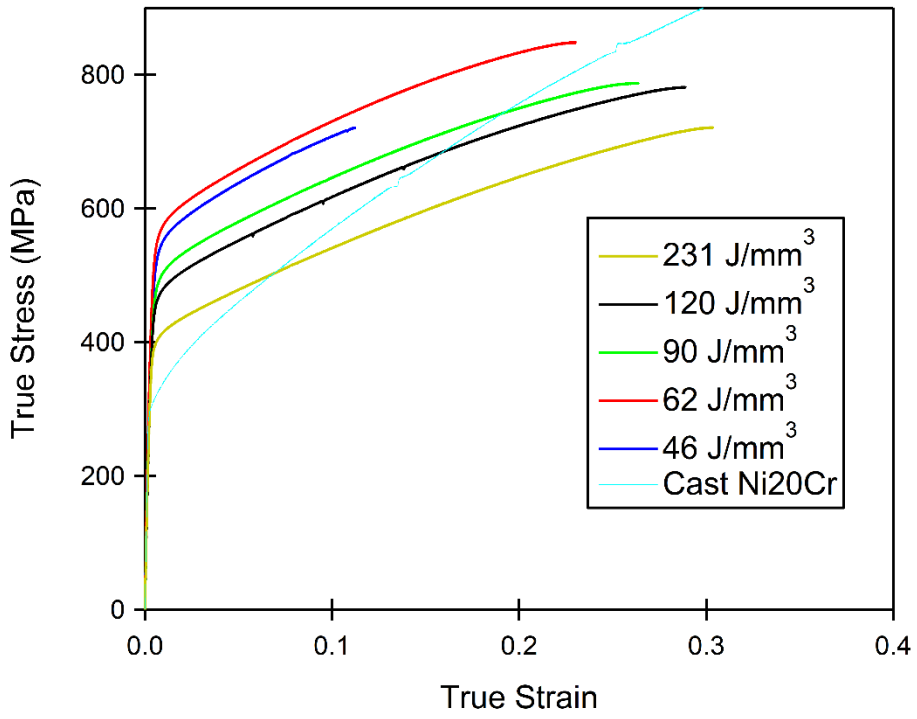

Figure 4: Monotonic tensile testing results in the 'True Stress-True Strain' framework of the LPBF Ni20Cr which are fabricated by volumetric energy of 46 J/mm^3, 62 J/mm^3 and 90 J/mm^3, 120 J/mm^3, and 231 J/mm^3 respectively.

3.3. Microstructure after interrupted tensile tests (5% strain)

Fig. 1 reveals the presence of Cr-rich precipitates for all volumetric energies. Generally, these precipitates are observed at the walls of dendritic cellular structures or inter-dendritic zones due to segregation of Cr, as shown in fig. 1. This location in dendrite walls may reduce their contribution to stress and strain hardening. In order to analyse the role played by such precipitates on plasticity and further model the microstructure contributions to yield stress and strain hardening accordingly, bright field TEM observations of dislocations after 5% of tensile strain were performed on sample 2 (62 J/mm^3). Fig. 5(a)-(c) represent field TEM micrographs of such strained samples in YZ plane (indicating upwards to the building direction). Firstly, in those figures, there are no evidences of mechanical twinning as already reported for this material [15]. Secondly, isolated dislocations can be observed as well as slip system trace as depicted by orange arrows. Finally, precipitates can be observed to interact with dislocations either by shearing or dislocation loop creation. Nevertheless, the occurrence of such dislocation interaction with precipitates is rather low and supposed to be of a second order compared to other dislocation-microstructure interactions. Precipitates may also indirectly influence the mechanical properties as they stabilize the dendritic cellular structures due to entanglement with initial dislocations.

This article has been published in Journal of Alloys and Compounds. The edited version of the article can be found here: https://doi.org/10.1016/j.jallcom.2023.172241

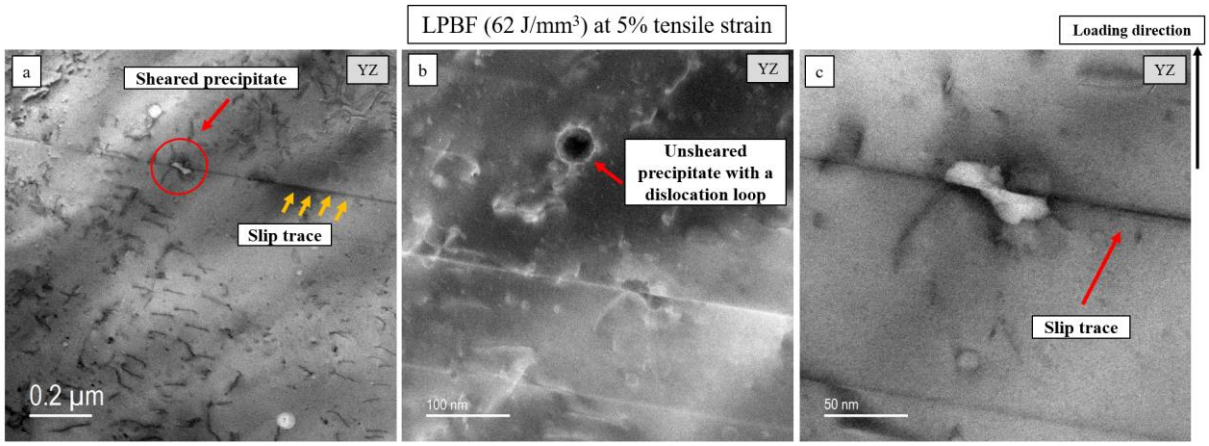

Figure 5: TEM micrographs (in YZ direction) of LPBF sample fabricated with 62 J/mm^3 loaded in tension till 5% strain showing (a) slip trace, precipitates (Cr-rich oxides) and dislocations (bright field), (b) magnified zone indicating sheared precipitate by a slip trace and unsheared precipitate surrounded by a dislocation loop (dark field/ DF2), and (c) further magnification of sheared precipitate (bright field). The loading direction is upwards and marked with an arrow.

3.4. Yield stress prediction

To calculate the contribution of each microstructure feature to the yield stress, multiscale microstructure characterization has been used. Following the analytical model proposed in a previous work *[15]*, the yield stress of the Ni20Cr samples can be estimated using equation 5, all terms being explained in table 5. In that case, following the previous section, mechanical twinning and precipitation were not considered as potential yield stress source.

$$\sigma^{y} = \sigma_{s.s.} + \alpha M \mu b \sqrt{\rho_s} + \frac{k_{HP}}{\sqrt{d}} + f_g K_s \frac{\mu b M}{l_0} \quad (5)$$

Table 5: Summary of the values of the different parameters of the Kock-Mecking model identified from modelling of the experimental tensile curves

Right hand term	Contribution type	Details
$\sigma_{s.s.}$	Solid solution contribution	• Estimated using recrystallized cast tensile data [42][43] = 115 MPa
$\alpha M \mu b \sqrt{\rho_s}$	Contribution of the regularly spaced defects	• Defects like isolated dislocations, small precipitates • Associated to dislocations in the soft zones ρ_s (inside the dendritic cells) • α : parameter considering dislocation interaction = 0.3 [21] • M: Taylor factor = 3 (average value taken from EBSD analysis of LPBF samples) • µ = Shear modulus = 8.1×10^4 MPa [44]
$\frac{k_{HP}}{\sqrt{d}}$	Grain size strengthening	• k_{HP} = slope of the Hall-Petch plot for yield stress • k_{HP} = 950 MPa.µm$^{-1/2}$ for cast [43] and LPBF [18] Ni20Cr
$f_g K_s \frac{\mu b M}{l_0}$	Dendrite long range backstress	• f_g: volume fraction of grains with hard zones = 1 (all grains reveal cell structures in LPBF metals)

This article has been published in Journal of Alloys and Compounds. The edited version of the article can be found here: https://doi.org/10.1016/j.jallcom.2023.172241

		• $l_{0:}$ average hard zones spacing (dendritic cellular spacing) • K_s: constant depending on the SFE = 2 for LPBF Ni20Cr [9] • μ: 8.1×10^4 MPa= Shear modulus; value taken from literature [45] • b: 0.25 nm = Burgers vector modulus; value taken from literature [46]

For this modelling, most of the parameters can be obtained using literature data (see table 5) except three microstructural parameters which have to be estimated, the dislocation density in the soft zone ρ_s, the grain size d as well as the dendrite size l_0. For the last two parameters, values obtained in the previous sections can be employed. The measurement of the dislocation density in the soft zones has been performed by TEM analysis for a VED of 62 J/mm^3. An average value of dislocation in soft zones $\rho_s = 4 \times 10^7$ /mm^2 was obtained applying a line network-based technique based on dislocation intercepts at five separate places [46]-[47]. This value of dislocation density has been extracted from a previous work [15]. This dislocation density was calculated using an average foil thickness of 200 nm [15]. As observed in fig. 3, the dislocation density in soft zones seem to be qualitatively similar for the sample with the lowest and highest VED. Consequently, we assumed, in first approximation, the same value of ρ_s for all samples. Nevertheless, this value of ρ_s is sensitive to the foil thickness, location of the samples considered for microscopic characterisation, hence it might induce some scattering. So we believe that difference between the experimental values of ρ_s for all the samples built with different VEDs will be lower than that of such scattering. K_g (a value of 5) was considered from literature [44].

Following eq. 5, material parameters values summarized in table 5 as well as microstructural characterization, the yield stress has been estimated for all VEDs. Results are provided in table 6. As it only depends on chemistry, the solid solution contribution was calculated to be 115 MPa using cast material data and is applicable for all other samples. Then, regarding the contribution of dislocation density in soft zones to yield stress, as explained above, a similar value of about 111 MPa for LPBF fabricated via VED of 62 J/mm^3 was applied for all the Ni20Cr LPBF samples.

When it comes to the grain size strengthening, it was observed to be highest (170 MPa) for 46 J/mm^3 due to smaller grain size (30 µm) and this factor tends to decrease with increment in the VED, eventually the lowest contribution of 66 MPa was computed for 231 J/mm^3 due to largest size of grains (200 µm). Final contribution of dendritic cellular structures is associated with their sizes (as given in table 3 (dendrite size)) as a matter of inverse proportionality. Highest contribution due to dendritic cellular structures has been calculated for 46 J/mm^3 due to smallest size of dendrite and follows a descending trend with increasing VED due to increment in the size of such dendrites. All the values are given with associated errors (90% of confidence interval). Total yield stress was summed up considering all the contributions and this prediction was found to be 33.2% higher for 46 J/mm^3 LPBF sample than its respective experimental YS value as given in table 6. For LPBF samples with 62 and 90 J/mm^3, the predicted YS values were about 7.5% higher than the experimental value. Whereas for 120 and 231 J/mm3 samples, the predicted YS values were just about 4.6% and 4% away from their respective experimental

values. For all the LPBF samples except for 46 J/mm^3, prediction of YS values is comparable to the experimental ones, indicating robustness of the employed model. In particular, higher the VED, better is the agreement between the predicted and experimental values of YS. For the 46 J/mm^3 LPBF sample, the issue could be associated with the necessity of correction of the effective experimental sections of samples. Indeed, the real stress could be higher than estimated one as porosity is not taken into account. Moreover, lower VED values are associated with higher cooling rates involved in the processing inducing higher residual stresses in the built components [49]. Moreover, Simson et al. [50] explain that impact of residual stress is even higher for samples with density lower than 99%, which is the case for LPFB samples with 46 J/mm^3. Relatively lower energy density might induce inadequate energy penetration inducing weak inter-layer bonding [50]. Hence, these higher residual stresses found for sample built with 46 J/mm^3 could be the reason for lower degree of agreement in predicted and experimental YS values.

These results clearly show that, except for the larger volumetric energy, the contribution of dendritic cellular structures over the yield stress is the most important which is about twice to that of contribution of the grain size. When high yield stress components are required, tailoring small dendrite owing to low VED is the best strategy no matter are the laser power or speed.

Table 6: Summary of the microstructural contributions (MPa) to the yield stress for LPBF samples.

VED (J/mm^3)	Solid solution	Dislocation density in soft zones	Grain size strengthening	Dendrite strengthening	Total YS predicted	YS experiment	Average error in prediction (%)
46	115	111	170	304 ± 36	698 ± 36	524 ± 12	33.2
62	115	111	111	259 ± 25	596 ± 25	554 ± 9	7.5
90	115	111	93	217 ± 85	536 ± 85	501 ± 9	6.9
120	115	111	82	192 ± 65	499 ± 65	477 ± 9	4.6
231	115	111	66	113 ± 13	404 ± 13	421 ± 14	4.0

Fig. 6 specifies the contribution (%) of the different microstructural features on predicted YS values for all the LPBF samples. Highest contribution is noticed for dendritic cellular structures irrespective of volumetric energy (contribution ranging between 40 and 50%), with lower contributions of other features. Interesting to note that dendrite contribution increases to 52% for 90 J/mm^3 and then reduces till 231 J/mm^3.

Homogenised cast Ni20Cr samples achieved experimental values of yield stress of 267±44 MPa which was considered as a reference in this work. The features that contribute to YS are solid solution (115 MPa), grain size (60 MPa according to EBSD analysis, as shown in previous work [15]), and the rest due to other mechanisms. Such mechanisms could be associated with initial dislocation density (due to thermal effects, samples will not be dislocation free even after homogenisation) and Short-Range Order (as Ni20Cr is prone to the formation of SRO [51],

[52]). We have not measured the dislocation density of cast sample, as this is outside the purview of this paper.

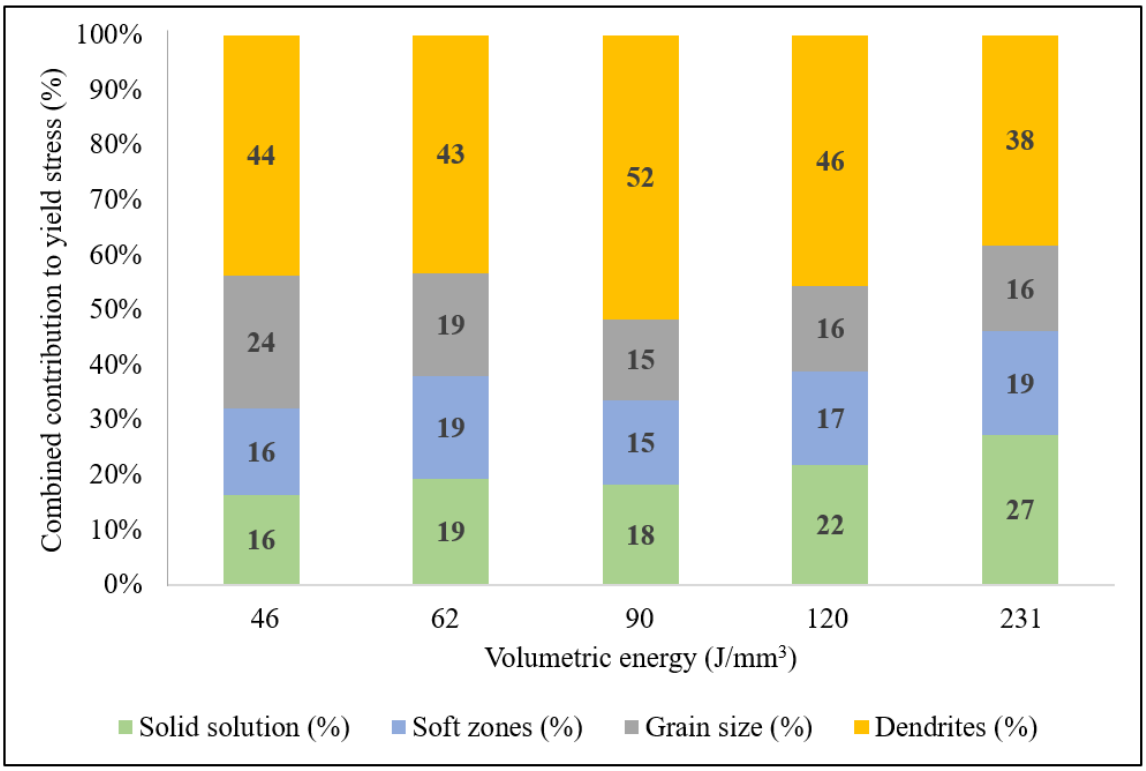

Figure 6: Stacked bar graphs indicating the contribution in percentage of solid solution, dislocation density in soft zones, grain size and dendrite strengthening on predicted yield stress of Ni20Cr LPBF samples fabricated by volumetric energy of 46 J/mm^3, 62 J/mm^3 and 90 J/mm^3, 120 J/mm^3, and 231 J/mm^3 respectively.

3.5. Kocks-Mecking modelling of the tensile behaviour

Using the tensile curves of all LPBF (all VEDs) and cast samples were used to establish the KM model. Microstructural analysis performed in the previous sections and information from literature presented table 5 has been utilized to solve eq. 2 and 3 (derivative of dislocation density with plastic strain). From a microstructural point of view, LPBF samples exhibit dendritic cellular structure associated to dislocation cells with high initial dislocation density, unlike in cast specimens. Hence contribution of initial dislocation structures is only valid for LPBF samples, whereas contribution of forest dislocation interaction, dislocation annihilation, grain size is valid for both LPBF and cast samples. As the sample can be considered as bulk ones, no surface effects are expected. For Ni20Cr LPBF, there are no evidence of extended mechanical twinning [15]. Consequently, the last two terms of eq. 3 are dismissed in the case of this study. Further, the contribution of precipitates network to strain hardening is also dismissed following the results of section 3. Finally, equation 3 can be written following eq. 6 for cast and eq. 7 for LPBF:

$$\frac{d\rho}{d\epsilon_p}^{cast} = \frac{M\sqrt{\rho}}{\beta b} + \frac{Mk_g}{bd} - K_2\rho \quad (6)$$

This article has been published in Journal of Alloys and Compounds. The edited version of the article can be found here: https://doi.org/10.1016/j.jallcom.2023.172241

$$\frac{d\rho}{d\epsilon_p}^{LPBF} = \frac{M\sqrt{\rho}}{\beta b} + \frac{Mk_g}{bd} - K_2\rho + \frac{M}{bl_0} \quad (7)$$

Taking into account these different microstructure contributions to strain hardening, three parameters have to be numerically optimized and identified: β, K_2 and l_0. Nevertheless, as mentioned in section 3.4, K_2 associated to dislocation annihilation, depends mostly on chemistry and temperature tests. A similar value of 0.97 already characterized for 62 J/mm^3 has been applied for all samples in a previous work [15].

Table 7: Summary of the values of the different parameters of the Kock-Mecking model identified from modelling of the experimental tensile curves.

Volumetric energy (J/mm^3)	**Grain size (µm)**	**β**	**K_2**	**l_0 (model) (µm)**	**Dendritic cell size (l_0) (exp) (µm)**	**Ratio of $l_{0(model)}$ to $l_{0(exp)}$**
231	200	1.56E+02	0.97 ± 0.12	6.3	1.1 ± 0.2	5.83
120	130	5.83E+09	0.97 ± 0.12	2.8	0.63 ± 0.2	4.44
90	100	3.91E+09	0.97 ± 0.12	2.5	0.56 ± 0.2	4.46
62	70	2.92E+09	0.97 ± 0.12	1.6	0.47 ± 0.05	3.40
46	30	4.07E+09	0.97 ± 0.12	1.3	0.40 ± 0.05	3.29
Cast Sample	400	40.8	1.69 ± 0.29	N.A.	N.A.	N.A.

Solving the two non-linear differential equations of KM model (eq. 2 and 7), with information from table 5, tensile curves were modelled and are shown in fig. 7 and also compared with the experimental curves. The model seems to be able to reproduce tensile behaviour correctly. Table 7 summarizes the values of β and l_0 optimized for all VEDs as well as the actual dendrite size ($\boldsymbol{l_0}$) and grain size of all LPBF samples as well as cast sample (cast values are extracted from previous study [15]). When it comes to β, reported values of cast and LPBF samples produced with the highest volumetric energy are of the same order of magnitude. For all other VEDs, this parameter demonstrating enormous values, reveals a neglectable contribution of forest dislocation interactions. Regarding the dendrite size ($\boldsymbol{l_0}$), both actual and predicted values are in the same order of magnitude proving the relevance of KM modelling. The predicted one is always larger than the actual one (factor between 3 and 5) revealing that the formulation of dendrite contribution to strain hardening returns overestimated values. Indeed, eq. 7 is based on theoretical aspects of plasticity which do not take into account the fact a dislocation interacting with dendrite walls will not always lead to dislocation production due to the different strength of the dislocation junctions [53].

This article has been published in Journal of Alloys and Compounds. The edited version of the article can be found here: https://doi.org/10.1016/j.jallcom.2023.172241

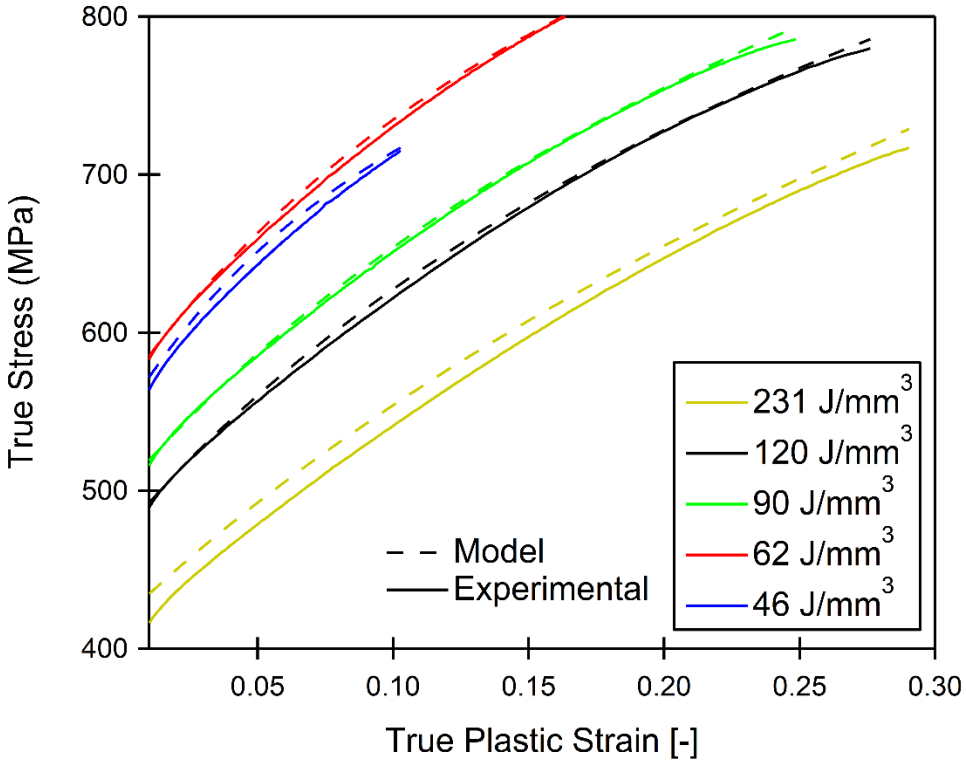

Figure 7: Comparison of the experimental and predicted tensile curves using Kock-Mecking model for LPBF Ni20Cr samples fabricated with volumetric energy of 46 J/mm3, 62 J/mm3 and 90 J/mm3, 120 J/mm3, and 231 J/mm3 respectively.

In order to quantify the contribution of LPBF Ni20Cr microstructure on strain hardening, optimized value of β and l_0 as well as the dislocation density evolution against strain have been employed to compute the different strain hardening mechanisms. These mechanisms are nothing but the individual 'terms' on the right-hand side of eq. 6 and 7.

Fig. illustrates the dislocation production rates via dendritic cellular structures (fig. 8(a)), grains (fig. 8(b)) and forest dislocations (fig. 8(c)) for all the samples. As for yield stress, dislocation production via dendritic cellular structures is the most significant contribution for strengthening of LPBF samples as higher magnitude of values were obtained than that of grain contribution and forest dislocation contribution. This rate reduces with increasing volumetric energies because of increment in the dendrite size. Dislocation production rate via grain size contributes for strengthening but relatively lower contribution than that of dendritic cellular structures, and shows same trend as the latter. It can be noted that owing to its independence to dislocation density, dislocation production rate via dendritic cellular structures and grain is constant and does not change with plastic strain. Dislocation production rate via forest dislocations is inoperative for LPBF samples with all volumetric energies (as seen in (fig. 8(c)), except for 231 J/mm^3, in agreement with the very large value of β (see table 7). For highest VED sample, this contribution is active and has maximum influence on strengthening in cast Ni20Cr samples.

This article has been published in Journal of Alloys and Compounds. The edited version of the article can be found here: https://doi.org/10.1016/j.jallcom.2023.172241

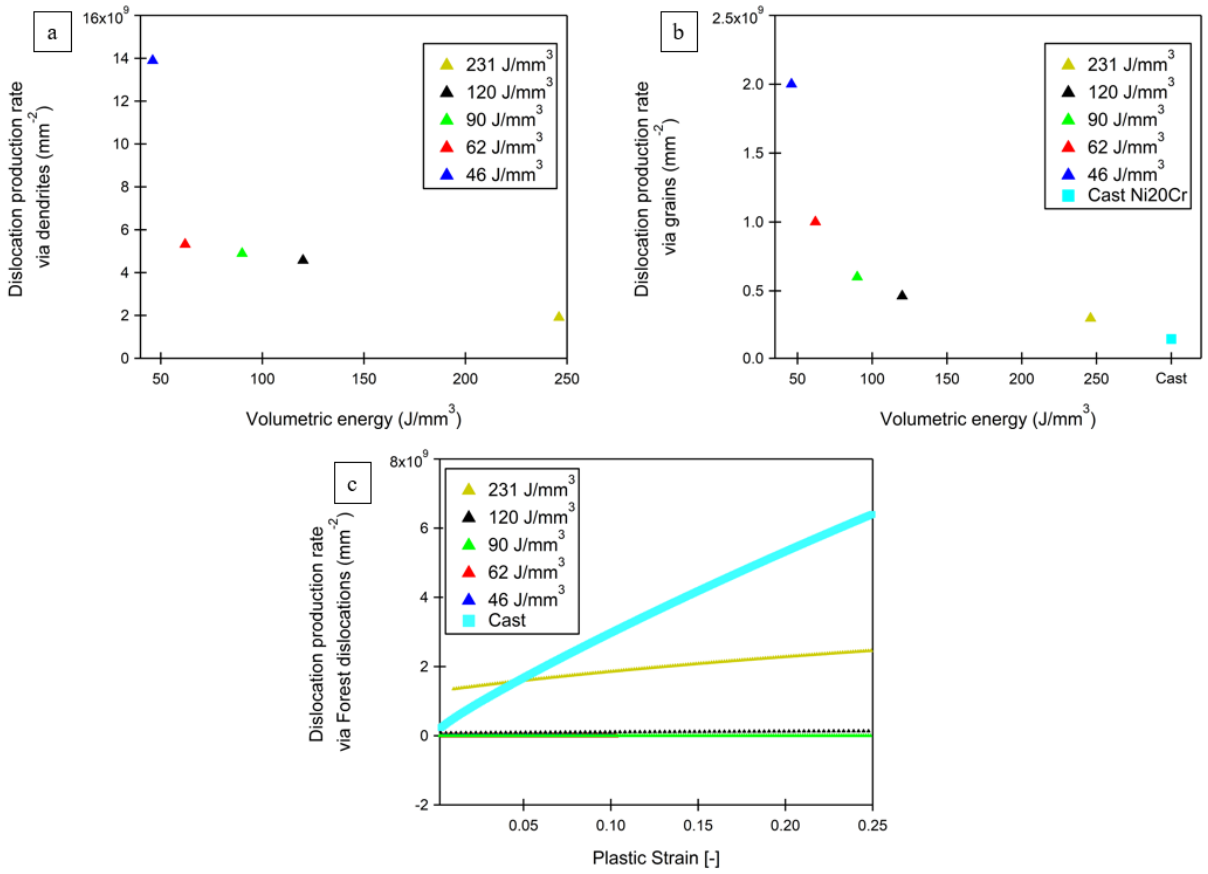

Figure 8: Dislocation production rate maps for the LPBF and cast Ni20Cr due to the contribution of (a) dendritic cellular structures and (b) grain size against all the volumetric energies. (c) Evolution of dislocation production rate with respect to plastic strain for all LPBF and cast Ni20Cr samples.

Due to its rather high dendrite size, dislocation production rate mechanisms seem to be modified for the highest VED. As observed in figure 8(c), forest dislocations mechanism for dislocation production rate seems significant, with almost equal fraction of contribution as in dendritic cellular structures. However, grain size contribution is the least out of all mechanisms studied for this sample. Initially, dendritic cellular structures seem to be the most significant for dislocation production but with increasing plastic strain, forest dislocations interactions become more substantial for this particular sample.

3.6. Correction factor in Kocks-Mecking model

So far, the dendritic cellular size associated in the functioning of the model was optimised and obtained as an output. However, such a KM model is also widely employed in crystal plasticity modelling using finite element model code for the prediction of mechanics of materials [54]–[57]. Such an approach of crystal plasticity modelling (FEM) needs experimental dendritic cellular size as an input for predicting the mechanical behaviour of additively manufactured materials. Ma et al. employed the Orowan equation to investigate the grain boundary-dislocations interaction using an crystal plasticity FEM approach [58]. Similar method has been reported in various studies [59]–[61]. Hence the objective of this section is to adapt the formulation of the model in order to take the dendrite size as an input. We observed in the previous section that the in fact the formulation of the model was not correct because the

This article has been published in Journal of Alloys and Compounds. The edited version of the article can be found here: https://doi.org/10.1016/j.jallcom.2023.172241

dendrite size predicted by the model was larger than the actual experimental value. Hence, we considered a correction factor to be more accurate and wide employability of this approach. This correction factor, δ, is then introduced in a modified dislocation production equation (eq. 8) and set to the average of the invert of the ratio of dendrite values predicted by the model and analysed experimentally for all VEDs. Such a value was computed from table 7 to about 0.22. A modified equation based on the aforementioned points has been proposed as eq. 8.

$$\frac{d\rho}{d\epsilon_p}^{AM} = \frac{M\sqrt{\rho}}{\beta b} + \frac{Mk_g}{bd} - K2\rho + \frac{\delta M}{bl_0} \quad (8)$$

Moreover, an uncertain aspect of the aforementioned KM model employed in the previous work is based on optimization of several parameters as dendritic cellular size (already explained in the previous paragraph), β and K_2. The previous work gives out an average value of K_2 equal to 0.97 for LPBF specimens, the model we employed in this work for validation for several VEDs, replaces the optimization of K_2 with this average value. Moreover, using a correction factor, experimental value of dendrite could be used. These modifications leave solely the 'β' parameter for optimization for dislocation production mechanisms.

Solving the two non-linear differential equations of the modified KM model (eq. 2 and 8) with parameter values from table 5, it is possible to reproduce tensile curves for all the VEDs (as seen in fig. 7) which confirms its validation and employability for LPBF samples.

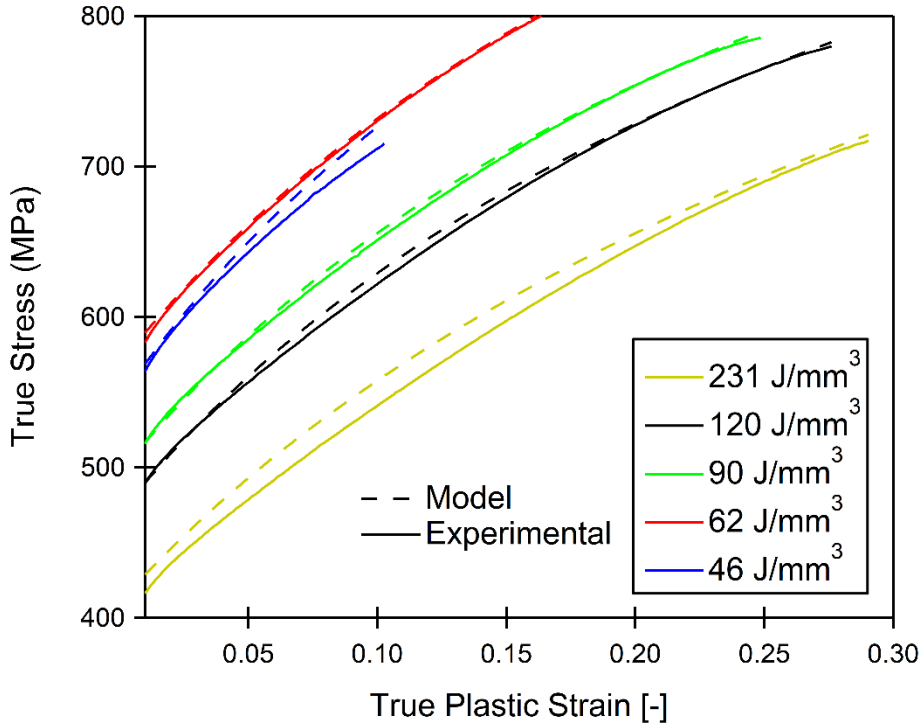

Figure 9: Comparison of the experimental and predicted tensile curves using Kock-Mecking model using a correction factor for dendrite production for LPBF Ni20Cr samples.

Despite introduction of such a correction factor, a perspective of this work could be a detailed microstructural analysis of all the LPBF samples (all VEDs) under TEM to study the influence of dendrite wall thickness, precipitate size and shape, shearing of precipitates as a function of Volumetric energy density.

This article has been published in Journal of Alloys and Compounds. The edited version of the article can be found here: https://doi.org/10.1016/j.jallcom.2023.172241

4. Conclusions

The objective of this work was to quantify the contribution of microstructural features using a Ni20Cr alloy manufactured with LPBF. The manufacturing was carried out with several volumetric energy densities to associate with such features. The work was based on analytical modelling, specifically the Kocks-Mecking formalism, and the relationship between the basic microstructural characteristics and flow stress as well as strain hardening for AM alloys has now been defined for several process parameters. The following are the key conclusions of this work:

- Combined mechanical testing, microstructure investigation and modelling is necessary to estimate contribution of AM length scales on mechanical behaviour.
- Analytical modelling based on microstructure (Taylor and Kocks-Mecking models) are able to reproduce LPBF behaviour for all volumetric energies.
- Contribution of LPBF microstructure features estimated, dendritic cellular structures responsible for ~45% of yield stress (62 J/mm^3, 90 J/mm^3, and 120 J/mm^3) and seem to fully control strain hardening.
- For LPBF Ni20Cr samples fabricated via 231 J/mm^3, forest dislocation interaction becomes responsible for dislocation production impacting strain hardening.
- A modified equation has been proposed with a correction factor (δ) of 0.22 and a constant value of K2 (0.97) for better employability of the model even in FEM framework by directly considering the input values of dendritic cellular structures.

Acknowledgement

The Labex EMC3 is greatly acknowledged for the financial support of the Nichrofab project. Authors also acknowledge the contribution of Dr Maxime Lelièvre for conducting monotonic tensile tests.

References

[1] W. Lefebvre, G. Rose, P. Delroisse, E. Baustert, F. Cuvilly, and A. Simar, “Nanoscale periodic gradients generated by laser powder bed fusion of an AlSi10Mg alloy,” *Materials & Design*, vol. 197, p. 109264, Jan. 2021, doi: 10.1016/j.matdes.2020.109264.

[2] B. Blakey-Milner *et al.*, “Metal additive manufacturing in aerospace: A review,” *Materials & Design*, vol. 209, p. 110008, Nov. 2021, doi: 10.1016/j.matdes.2021.110008.

[3] Z. Wu, S. R. Yarasi, J. Seo, N. Lamprinakos, and A. D. Rollett, “Study of the Printability, Microstructures, and Mechanical Performances of Laser Powder Bed Fusion Built Haynes 230,” *Metals*, vol. 12, no. 8, Art. no. 8, Aug. 2022, doi: 10.3390/met12081380.

[4] A. Leicht, M. Rashidi, U. Klement, and E. Hryha, “Effect of process parameters on the microstructure, tensile strength and productivity of 316L parts produced by laser powder bed fusion,” *Materials Characterization*, vol. 159, p. 110016, Jan. 2020, doi: 10.1016/j.matchar.2019.110016.

[5] Č. Donik, J. Kraner, I. Paulin, and M. Godec, “Influence of the Energy Density for Selective Laser Melting on the Microstructure and Mechanical Properties of Stainless Steel,” *Metals*, vol. 10, no. 7, Art. no. 7, Jul. 2020, doi: 10.3390/met10070919.

This article has been published in Journal of Alloys and Compounds. The edited version of the article can be found here: https://doi.org/10.1016/j.jallcom.2023.172241

[6] O. Andreau *et al.*, “Texture control of 316L parts by modulation of the melt pool morphology in selective laser melting,” *Journal of Materials Processing Technology*, vol. 264, pp. 21–31, Feb. 2019, doi: 10.1016/j.jmatprotec.2018.08.049.
[7] S. Griffiths, M. D. Rossell, J. Croteau, N. Q. Vo, D. C. Dunand, and C. Leinenbach, “Effect of laser rescanning on the grain microstructure of a selective laser melted Al-Mg-Zr alloy,” *Materials Characterization*, vol. 143, pp. 34–42, Sep. 2018, doi: 10.1016/j.matchar.2018.03.033.
[8] M. Godec, S. Zaefferer, B. Podgornik, M. Šinko, and E. Tchernychova, “Quantitative multiscale correlative microstructure analysis of additive manufacturing of stainless steel 316L processed by selective laser melting,” *Materials Characterization*, vol. 160, p. 110074, Feb. 2020, doi: 10.1016/j.matchar.2019.110074.
[9] B. Stegman *et al.*, “Volumetric energy density impact on mechanical properties of additively manufactured 718 Ni alloy,” *Materials Science and Engineering: A*, vol. 854, p. 143699, Sep. 2022, doi: 10.1016/j.msea.2022.143699.
[10] T. Yang *et al.*, “Laser powder bed fusion of AlSi10Mg: Influence of energy intensities on spatter and porosity evolution, microstructure and mechanical properties,” *Journal of Alloys and Compounds*, vol. 849, p. 156300, Dec. 2020, doi: 10.1016/j.jallcom.2020.156300.
[11] T. Kimura, T. Nakamoto, T. Ozaki, and T. Miki, “Microstructures and mechanical properties of aluminum-transition metal binary alloys (Al-Fe, Al-Mn, and Al-Cr) processed by laser powder bed fusion,” *Journal of Alloys and Compounds*, vol. 872, p. 159680, Aug. 2021, doi: 10.1016/j.jallcom.2021.159680.
[12] W. Chen, Q. Yang, S. Huang, S. Huang, J. J. Kruzic, and X. Li, “Laser power modulated microstructure evolution, phase transformation and mechanical properties in NiTi fabricated by laser powder bed fusion,” *Journal of Alloys and Compounds*, vol. 861, p. 157959, Apr. 2021, doi: 10.1016/j.jallcom.2020.157959.
[13] X. Tang *et al.*, “A study on the mechanical and electrical properties of high-strength CuCrZr alloy fabricated using laser powder bed fusion,” *Journal of Alloys and Compounds*, vol. 924, p. 166627, Nov. 2022, doi: 10.1016/j.jallcom.2022.166627.
[14] G. V. de Leon Nope, L. I. Perez-Andrade, J. Corona-Castuera, D. G. Espinosa-Arbelaez, J. Muñoz-Saldaña, and J. M. Alvarado-Orozco, “Study of volumetric energy density limitations on the IN718 mesostructure and microstructure in laser powder bed fusion process,” *Journal of Manufacturing Processes*, vol. 64, pp. 1261–1272, Apr. 2021, doi: 10.1016/j.jmapro.2021.02.043.
[15] S. S. Joshi, C. Keller, L. Mas, W. Lefebvre, E. Hug, and J.-P. Couzinie, “On the origin of the strain hardening mechanisms of Ni20Cr alloy manufactured by laser powder bed fusion,” *International Journal of Plasticity*, vol. 165, p. 103610, Jun. 2023, doi: 10.1016/j.ijplas.2023.103610.
[16] B. Song, S. Dong, P. Coddet, H. Liao, and C. Coddet, “Fabrication of NiCr alloy parts by selective laser melting: Columnar microstructure and anisotropic mechanical behavior,” *Materials & Design*, vol. 53, pp. 1–7, Jan. 2014, doi: 10.1016/j.matdes.2013.07.010.
[17] S. Das, J. B. Seol, Y. C. Kim, and C. G. Park, “Structure and mechanical properties of Ni–Cr alloy produced by single roll strip casting,” *Materials & Design*, vol. 31, no. 1, pp. 570–573, Jan. 2010, doi: 10.1016/j.matdes.2009.07.006.
[18] E. Hug, M. Lelièvre, C. Folton, A. Ribet, M. Martinez-Celis, and C. Keller, “Additive manufacturing of a Ni-20 wt%Cr binary alloy by laser powder bed fusion: Impact of the microstructure on the mechanical properties,” *Materials Science and Engineering: A*, vol. 834, p. 142625, Feb. 2022, doi: 10.1016/j.msea.2022.142625.
[19] J. Schindelin *et al.*, “Fiji: an open-source platform for biological-image analysis,” *Nat Methods*, vol. 9, no. 7, Art. no. 7, Jul. 2012, doi: 10.1038/nmeth.2019.
[20] H. Mecking, U. F. Kocks, and H. Fischer, *Hardening, recovery, and creep in fcc mono- and polycrystals*. 1976. Accessed: May 04, 2022. [Online]. Available: https://ui.adsabs.harvard.edu/abs/1976sma..conf.....M

This article has been published in Journal of Alloys and Compounds. The edited version of the article can be found here: https://doi.org/10.1016/j.jallcom.2023.172241

[21] U. F. Kocks and H. Mecking, “Physics and phenomenology of strain hardening: the FCC case,” *Progress in Materials Science*, vol. 48, no. 3, pp. 171–273, Jan. 2003, doi: 10.1016/S0079-6425(02)00003-8.
[22] U. Essmann and H. Mughrabi, “Annihilation of dislocations during tensile and cyclic deformation and limits of dislocation densities,” *Philosophical Magazine A*, vol. 40, no. 6, pp. 731–756, Dec. 1979, doi: 10.1080/01418617908234871.
[23] D. R. Steinmetz *et al.*, “Revealing the strain-hardening behavior of twinning-induced plasticity steels: Theory, simulations, experiments,” *Acta Materialia*, vol. 61, no. 2, pp. 494–510, Jan. 2013, doi: 10.1016/j.actamat.2012.09.064.
[24] T. Narutani and J. Takamura, “Grain-size strengthening in terms of dislocation density measured by resistivity,” *Acta Metallurgica et Materialia*, vol. 39, no. 8, pp. 2037–2049, Aug. 1991, doi: 10.1016/0956-7151(91)90173-X.
[25] U. Essmann, M. Rapp, and M. Wilkens, “Die versetzungsanordnung in plastisch verformten kupfer-vielkristallen,” *Acta Metallurgica*, vol. 16, no. 10, pp. 1275–1287, Oct. 1968, doi: 10.1016/0001-6160(68)90008-4.
[26] H. Mecking, “Description of hardening curves of fcc single- and polycrystals,” Argonne National Lab., Ill. (USA), CONF-751164-3, Jan. 1975. Accessed: May 04, 2022. [Online]. Available: https://www.osti.gov/biblio/7272466
[27] H. Mecking and U. F. Kocks, “Kinetics of flow and strain-hardening,” *Acta Metallurgica*, vol. 29, no. 11, pp. 1865–1875, Nov. 1981, doi: 10.1016/0001-6160(81)90112-7.
[28] D. Kuhlmann-Wilsdorf, “Theory of plastic deformation: - properties of low energy dislocation structures,” *Materials Science and Engineering: A*, vol. 113, pp. 1–41, Jul. 1989, doi: 10.1016/0921-5093(89)90290-6.
[29] R. E. Smallman and A. H. W. Ngan, “Mechanical properties I,” in *Physical Metallurgy and Advanced Materials*, Butterworth-Heinemann, 2007, pp. 289–381.
[30] J. Gil Sevillano, “The Cold Worked State,” *MSF*, vol. 113–115, pp. 19–28, Jan. 1993, doi: 10.4028/www.scientific.net/MSF.113-115.19.
[31] X. Feaugas, “On the origin of the tensile flow stress in the stainless steel AISI 316L at 300 K: back stress and effective stress,” *Acta Materialia*, vol. 47, no. 13, pp. 3617–3632, Oct. 1999, doi: 10.1016/S1359-6454(99)00222-0.
[32] L. Kubin, T. Hoc, and B. Devincre, “Dynamic recovery and its orientation dependence in face-centered cubic crystals,” *Acta Materialia*, vol. 57, no. 8, pp. 2567–2575, May 2009, doi: 10.1016/j.actamat.2009.02.013.
[33] S. Bahl, S. Mishra, K. U. Yazar, I. R. Kola, K. Chatterjee, and S. Suwas, “Non-equilibrium microstructure, crystallographic texture and morphological texture synergistically result in unusual mechanical properties of 3D printed 316L stainless steel,” *Additive Manufacturing*, vol. 28, pp. 65–77, Aug. 2019, doi: 10.1016/j.addma.2019.04.016.
[34] C. Keller and E. Hug, “Kocks-Mecking analysis of the size effects on the mechanical behavior of nickel polycrystals,” *International Journal of Plasticity*, vol. 98, pp. 106–122, Nov. 2017, doi: 10.1016/j.ijplas.2017.07.003.
[35] D. Kong, C. Dong, X. Ni, L. Zhang, and X. Li, “Cellular size dependence on the strength of additively manufactured austenitic stainless steel,” *Materials Letters*, vol. 279, p. 128524, Nov. 2020, doi: 10.1016/j.matlet.2020.128524.
[36] P. Petroušek *et al.*, “Investigation of the Properties of 316L Stainless Steel after AM and Heat Treatment,” *Materials*, vol. 16, no. 11, Art. no. 11, Jan. 2023, doi: 10.3390/ma16113935.
[37] R. R. Dehoff, M. M. Kirka, F. A. List, K. A. Unocic, and W. J. Sames, “Crystallographic texture engineering through novel melt strategies via electron beam melting: Inconel 718,” *Materials Science and Technology*, vol. 31, no. 8, pp. 939–944, Jun. 2015, doi: 10.1179/1743284714Y.0000000697.
[38] S. Dépinoy, “Influence of solidification conditions on chemical heterogeneities and dislocations patterning in additively manufactured 316L stainless steel,” *Materialia*, vol. 24, p. 101472, Aug. 2022, doi: 10.1016/j.mtla.2022.101472.

This article has been published in Journal of Alloys and Compounds. The edited version of the article can be found here: https://doi.org/10.1016/j.jallcom.2023.172241

[39] Z. Chen *et al.*, “Laser Powder Bed Fusion of K418 Superalloy: Process, Microstructure, Texture Feature, and Mechanical Property,” *Metals*, vol. 12, no. 4, Art. no. 4, Apr. 2022, doi: 10.3390/met12040611.
[40] M. J. Bermingham, D. H. StJohn, J. Krynen, S. Tedman-Jones, and M. S. Dargusch, “Promoting the columnar to equiaxed transition and grain refinement of titanium alloys during additive manufacturing,” *Acta Materialia*, vol. 168, pp. 261–274, Apr. 2019, doi: 10.1016/j.actamat.2019.02.020.
[41] X. Liu, R. Hu, X. Luo, C. Yang, and X. Gao, “A high-strength Ni–Cr–W based superalloy prepared by laser powder bed fusion: printability, microstructure and tensile properties,” *Materials Science and Engineering: A*, vol. 853, p. 143744, Sep. 2022, doi: 10.1016/j.msea.2022.143744.
[42] X. Feaugas and H. Haddou, “Grain-size effects on tensile behavior of nickel and AISI 316L stainless steel,” *Metall Mater Trans A*, vol. 34, no. 10, pp. 2329–2340, Oct. 2003, doi: 10.1007/s11661-003-0296-5.
[43] B. A. Wilcox and A. H. Clauer, “The role of grain size and shape in strengthening of dispersion hardened nickel alloys,” *Acta Metallurgica*, vol. 20, no. 5, pp. 743–757, May 1972, doi: 10.1016/0001-6160(72)90103-4.
[44] M. Rudloff, “Etude des mécanismes de transition volume/surface du comportement mécanique d’un alliage Ni20Cr,” p. 200.
[45] G. Calvarin-Amiri, R. Molins, and A. M. Huntz, “Effect of the Application of a Mechanical Load on the Oxide-Layer Microstructure and on the Oxidation Mechanism of Ni–20Cr Foils,” *Oxidation of Metals*, vol. 53, no. 3, pp. 399–426, Apr. 2000, doi: 10.1023/A:1004553623556.
[46] M. Z. Butt and U. Sattar, “Deformation behavior of nickel-chromium alloys with special reference to the nature of solute distribution,” *Journal of Materials Science Letters*, vol. 20, no. 8, pp. 759–761, Apr. 2001, doi: 10.1023/A:1010991816598.
[47] M. Fripan and H. Eckart Exner, “Three-Dimensional orientation and roughness of surfaces,” *Acta Stereol*, pp. 181–186, 1984.
[48] R. K. Ham, “The determination of dislocation densities in thin films,” *The Philosophical Magazine: A Journal of Theoretical Experimental and Applied Physics*, vol. 6, no. 69, pp. 1183–1184, Sep. 1961, doi: 10.1080/14786436108239679.
[49] T. Mishurova, K. Artzt, J. Haubrich, G. Requena, and G. Bruno, “Exploring the Correlation between Subsurface Residual Stresses and Manufacturing Parameters in Laser Powder Bed Fused Ti-6Al-4V,” *Metals*, vol. 9, no. 2, Art. no. 2, Feb. 2019, doi: 10.3390/met9020261.
[50] T. Simson, A. Emmel, A. Dwars, and J. Böhm, “Residual stress measurements on AISI 316L samples manufactured by selective laser melting,” *Additive Manufacturing*, vol. 17, pp. 183–189, Oct. 2017, doi: 10.1016/j.addma.2017.07.007.
[51] N. R. Dudova, R. O. Kaibyshev, and V. A. Valitov, “Short-range ordering and the abnormal mechanical properties of a Ni-20% Cr alloy,” *Phys. Metals Metallogr.*, vol. 108, no. 6, pp. 625–633, Dec. 2009, doi: 10.1134/S0031918X0912014X.
[52] N. R. Dudova and R. O. Kaibyshev, “Short-range ordering and mechanical properties of a Ni-20%Cr alloy,” *J. Phys.: Conf. Ser.*, vol. 240, p. 012081, Jul. 2010, doi: 10.1088/1742-6596/240/1/012081.
[53] M. Ben Bettaieb, O. Débordes, A. Dogui, L. Duchêne, and C. Keller, “On the numerical integration of rate independent single crystal behavior at large strain,” *International Journal of Plasticity*, vol. 32–33, pp. 184–217, May 2012, doi: 10.1016/j.ijplas.2011.10.010.
[54] C. Wang, Z. J. Li, C. Q. Ji, S. W. Gao, and Y. N. Cui, “Crystal plasticity analysis of the evolutions of temperature, stress and dislocation in additively manufactured tungsten,” *International Journal of Refractory Metals and Hard Materials*, vol. 110, p. 106041, Jan. 2023, doi: 10.1016/j.ijrmhm.2022.106041.
[55] X. X. Zhang *et al.*, “Multiscale constitutive modeling of additively manufactured Al–Si–Mg alloys based on measured phase stresses and dislocation density,” *International Journal of Plasticity*, vol. 140, p. 102972, May 2021, doi: 10.1016/j.ijplas.2021.102972.

This article has been published in Journal of Alloys and Compounds. The edited version of the article can be found here: https://doi.org/10.1016/j.jallcom.2023.172241

[56] H. Eskandari Sabzi, X.-H. Li, C. Zhang, H. Fu, and P. E. J. Rivera-Díaz-del-Castillo, “Strain hardening in twinning-induced plasticity stainless steel produced by laser powder bed fusion,” *Materials Science and Engineering: A*, vol. 855, p. 143882, Oct. 2022, doi: 10.1016/j.msea.2022.143882.
[57] J. Kwon, G. M. Karthik, Y. Estrin, and H. S. Kim, “Constitutive modeling of cellular-structured metals produced by additive manufacturing,” *Acta Materialia*, vol. 241, p. 118421, Dec. 2022, doi: 10.1016/j.actamat.2022.118421.
[58] A. Ma, F. Roters, and D. Raabe, “Studying the effect of grain boundaries in dislocation density based crystal-plasticity finite element simulations,” *International Journal of Solids and Structures*, vol. 43, no. 24, pp. 7287–7303, Nov. 2006, doi: 10.1016/j.ijsolstr.2006.07.006.
[59] A. Ma, F. Roters, and D. Raabe, “A dislocation density based constitutive model for crystal plasticity FEM including geometrically necessary dislocations,” *Acta Materialia*, vol. 54, no. 8, pp. 2169–2179, May 2006, doi: 10.1016/j.actamat.2006.01.005.
[60] A. Ma and F. Roters, “A constitutive model for fcc single crystals based on dislocation densities and its application to uniaxial compression of aluminium single crystals,” *Acta Materialia*, vol. 52, no. 12, pp. 3603–3612, Jul. 2004, doi: 10.1016/j.actamat.2004.04.012.
[61] F. Roters, “A new concept for the calculation of the mobile dislocation density in constitutive models of strain hardening,” *physica status solidi (b)*, vol. 240, no. 1, pp. 68–74, 2003, doi: 10.1002/pssb.200301873.

This article has been published in Journal of Alloys and Compounds. The edited version of the article can be found here: https://doi.org/10.1016/j.jallcom.2023.172241